
University of Bristol Thesis Template

Subtitle

By

AUTHOR'S NAME



Department of Engineering Mathematics
UNIVERSITY OF BRISTOL

A dissertation submitted to the University of Bristol in accordance with the requirements of the degree of DOCTOR OF PHILOSOPHY in the Faculty of Engineering.

APRIL 2013

Word count: ten thousand and four

ABSTRACT

Here goes the abstract

DEDICATION AND ACKNOWLEDGEMENTS

Here goes the dedication.

AUTHOR'S DECLARATION

I declare that the work in this dissertation was carried out in accordance with the requirements of the University's Regulations and Code of Practice for Research Degree Programmes and that it has not been submitted for any other academic award. Except where indicated by specific reference in the text, the work is the candidate's own work. Work done in collaboration with, or with the assistance of, others, is indicated as such. Any views expressed in the dissertation are those of the author.

SIGNED: DATE:

TABLE OF CONTENTS

	Page
List of Tables	ix
List of Figures	xi
1 Introduction	1
1.1 Non Linear Emission of Radiation in Liquid Xenon	1
1.2 EFT	3
2 Search For High Energy Nuclear Recoils in XENON100 Detector	5
2.1 Low energy channel	6
2.2 High energy channel	7
2.3 Signal model	9
2.3.1 Elastic scattering	10
2.3.2 Inelastic WIMP scattering	12
2.4 Statistical inference	12
2.5 Results	14
A EFT SIGNAL MODEL DETECTOR RESPONSE TABLE	19
Bibliography	23

LIST OF TABLES

TABLE	Page
2.1 Definitions and contents of the analysis bins for the high energy channel. The expected background counts are calculated by taking the calibration sample and scaling it by 6.54×10^{-3} , which is the ratio of observed counts to calibration counts in a sideband.	9
A.1 Detector response table using \mathcal{L}_{eff} with constrained scaling parameter set to -1σ value. First column gives recoil energies, subsequent columns give the values of $G'_i(E)$ for each of the 9 high-energy analysis bins. The sampling is in steps of 10 keV _{nr} , which is too coarse to give an accurate signal model for very low WIMP masses, but is suitable for the mass range most relevant to our analysis. Higher resolution $G'_i(E)$ functions, and $G'_i(E)$ functions for other values of \mathcal{L}_{eff} , are given in supplementary material.	20

LIST OF FIGURES

FIGURE	Page
1.1 TODO list of figures caption.	2
2.1 Summary of regions of interest, backgrounds, and observed data. ER calibration data, namely ^{60}Co and ^{232}Th data is shown as light cyan dots. NR calibration data ($^{241}\text{AmBe}$) is shown as light red dots. Dark matter search data is shown as black dots. The red line is the threshold between the low and high energy channels. The lines in blue are the bands. For the low-energy channel the bands are constructed to achieve constant expected signal density, and are operator and mass dependent, shown here for a $50 \text{ GeV}/c^2$ WIMP using the \mathcal{O}_1 operator. For the high-energy region, the nine analysis bins are presented also in blue lines.	6
2.2 The total acceptance of all cuts used. Data from calibration is shown in black, with a 3rd order polynomial fit in red.	8
2.3 The expected signal in the high energy region for a $300 \text{ GeV}/c^2$ WIMP mass, normalized to 5 events. Left(right) is the spectra for $O_1(O_6)$. Notice that for O_1 most of the events are not expected to deposit energy higher than 30 PE whereas for O_6 a large fraction of the events appear in this region.	11
2.4 The expected signal in the low energy region for a $300 \text{ GeV}/c^2$ WIMP mass, normalized to 5 events. Left(right) is the spectra for $\mathcal{O}_1(\mathcal{O}_6)$. Notice that for \mathcal{O}_1 most of the events are expected to deposit energy lower than 30 PE whereas for \mathcal{O}_6 a large fraction of the events do not appear in this region at all. The black lines indicate the bands constructed on these specific mass and operator models, and are dividing the signal into 8 equally distributed signal sub-regions. This parameter space can be mapped with a one to one mapping to the $(y - cS1)$ space.	11
2.5 The XENON100 limits (90% CL _S) on isoscalar dimensionless coupling for all elastic scattering EFT operators. The limits are indicated in solid black. The expected sensitivity is shown in green and yellow(1σ and 2σ respectively). Limits from CDMS-II Si, CDMS-II Ge, and SuperCDMS [1] are presented as blue asterisks, green triangles, and orange rectangles, respectively. For operator 3 and 8 a full limit was published, for all other operators only $m_\chi = 10$ and $m_\chi = 300$ are available.	15

LIST OF FIGURES

2.6	90% CL _S limits, for the inelastic model, on the magnitude of the coupling constant for \mathcal{O}_1 , reported as a function of the WIMP mass and mass splitting δ	16
2.7	The XENON100 90% CL _S limits on a 1 TeV/c ² WIMP isoscalar dimensionless coupling constant as function of the WIMP mass splitting δ_m for all inelastic scattering EFT operators. Limits are indicated in solid black. The expected sensitivity is shown in green and yellow (1 σ and 2 σ respectively). For \mathcal{O}_1 (SI) results from XENON100(red triangle) CDMS-II(blue rectangle) and ZEPLIN-III(black star) are overlaid.	17
A.1	A visualization of the detector response table for -1σ (i.e. conservative) \mathcal{L}_{eff} , as provided in the supplementary material. The y axis indicates the bins used for the high-energy signal region of this analysis (explained in 2.1). The x axis shows recoil energies, and the colors give the probability density for a recoil of a given recoil energy to produce an event in each analysis bin. To produce a signal model for this analysis, one simply multiplies the table values by dR/dE and integrates over E. The result is the predicted signal rate for each analysis bin.	21

INTRODUCTION

B egins

1.1 Non Linear Emission of Radiation in Liquid Xenon

As explained in (?? TODO add reference here) in LXe based experiment the exact properties of the scintillation and ionization responses to all types of interaction must be well quantified and understood. Mainly, much research has been focused on the scintillation and ionization responses of LXe to events with energy recoil as low as $<O(10\text{ keV})$ [2–4](TODO add LUX). Specifically the reconstruction of the directionality of recoil nuclei or electrons is of great interest to DM direct detection experiments. Better understanding of these properties may help to reduce background dramatically.

Several existing and proposed experiments such as DRIFT-II [5], DMTPC [6], NEWAGE [7] and MIMAC [8], exploit recoil direction properties. However These experiments are using dilute gas in which the ionization tracks extend to a few millimeters. However, in LXe the track length is estimated to be $O(100\text{nm})$. Moreover the topology of the excimers clouds is represented by a complex structure of branches which are formed by secondary recoils [35,50]. These two different properties, track length and structure, makes it highly difficult if not impossible to construct directionality in a LXe experiment. Therefore, a different approach for directionality measurement needs to be adopted for DM LXe based experiments.

The phenomena of an isolated particle in an excited state undergoing a transition to its ground state (i.e. spontaneous decay) as a result of the vacuum electromagnetic field is well described in the theory of quantum electrodynamics. This theory is applicable for an ensemble of particles only when particles interact with the vacuum electromagnetic field separately. In this case the ensemble will emit light an exponential law. The characteristic time, τ_{sp} , of a single

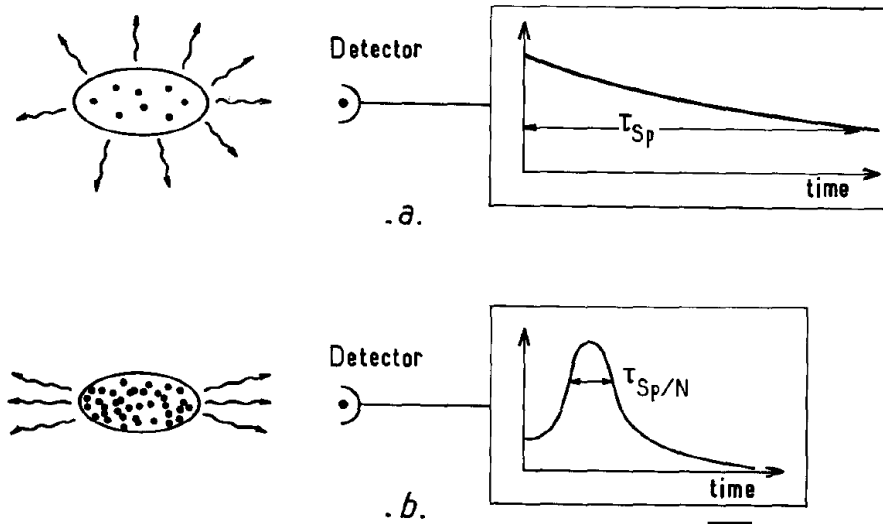


FIGURE 1.1. TODO insert caption here

particle to radiate is equal to the reciprocal of the transition rate Γ from the initially excited level. The radiation pattern in this case is isotropic in its nature, see Fig. 1.1a.

These radiation properties are significantly different when the radiating particles are dense enough. In this case the collective radiation from the ensemble is different than the sum of all particles radiating. This phenomena was first postulated by Dicke [9] in 1954 and was first measured in Xe by Rosenberger in 1965 [10]. In his research the radiation decay time from a two level atomic system was considered and expected to be dependent on the number of radiating particles N . This type of emission is referred as superradiance. This phenomena is due to interaction of the radiating particles with each other via a common electromagnetic radiation field, which results in a correlation between the atomic dipole moment. This correlation leads to a macroscopic optical polarization proportional to N . Hence the radiation intensity is proportional to N^2 , leading to a pulsed radiation with duration proportional to $1/N$, see Fig 1.1b. The phenomena of superradiance has been studied extensively since see [TODO add cite [52, 53]]

An effective self-induction of correlations between dipole moments is a necessary condition for a particles to exhibit a *superradiance* emission. The condition for this to occur are very different then the ones of regular fluorescence. The characteristic time of *superradiance* emission to happen, $\tau_c \sim 1/N$ must be shorter the relaxation time of the atomic dipole moment, τ_d . It also has to be shorter then τ_{sp} , however in most cases, τ_d is smaller than τ_{sp} , hence this is a more stirringit condition. Notice that unlike inverse population that happens in lasers, which occurs due to an external "pump", the correlation build-up between the radiating particles in *superradiance* happens spontaneously in the course of emission process.

The geometry of the radiating particle ensemble influences greatly weather or not a system

will exhibit a *superradiance* or standard spontaneous emissions. Specifically the two relevant quantities, are the wavelength λ of the emitted photon, and the size of the radiating particles cloud. A system with linear size much smaller than the emitted photons wavelength.

1.2 EFT

The traditional approach for computing predictions of the rate of WIMP-nucleon scattering has been to take only leading-order terms in a WIMP-nucleon effective field theory (EFT) with a very simple treatment of nuclear structure [11]. This leads to two main types of interactions, which are commonly labelled “Spin Independent” (SI) and “Spin Dependent” (SD). However, in recent years many authors have pointed out that in certain theories these interactions may be suppressed or nonexistent, such that otherwise subleading interactions may dominate the scattering process [12]. To account for this possibility in a systematic way, a more sophisticated EFT approach has been developed [13–15]. In the new approach, an effective Lagrangian describing the WIMP-nucleus interaction is constructed, that takes into account all Galilean-invariant operators up to second order in the momentum exchange. This framework introduces new operators associated with different types of nuclear responses, along with the standard SI and SD ones, resulting in a set of fourteen operators \mathcal{O}_i which may couple independently to protons and neutrons. In Eqs. (1.1) we list these operators following the convention from [14]. The operators depend explicitly on 4 linearly independent quantities: $\vec{v}^\perp \equiv \vec{v} + \frac{\vec{q}}{2\mu_N}$, the relative perpendicular velocity between the WIMP and the nucleon, \vec{q} , the momentum transferred in the scattering event, and \vec{S}_χ, \vec{S}_N , the WIMP and nucleon spins. \mathcal{O}_2 is not considered here as it cannot be obtained from a relativistic operator at leading order.

$$\begin{aligned}
\mathcal{O}_1 &= 1_\chi 1_N & \mathcal{O}_9 &= i\vec{S}_\chi \cdot (\vec{S}_N \times \frac{\vec{q}}{m_N}) \\
\mathcal{O}_3 &= i\vec{S}_N \cdot (\frac{\vec{q}}{m_N} \times \vec{v}^\perp) & \mathcal{O}_{10} &= i\vec{S}_N \cdot (\frac{\vec{q}}{m_N}) \\
\mathcal{O}_4 &= \vec{S}_\chi \cdot \vec{S}_N & \mathcal{O}_{11} &= i\vec{S}_\chi \cdot (\frac{\vec{q}}{m_N}) \\
\mathcal{O}_5 &= i\vec{S}_\chi \cdot (\frac{\vec{q}}{m_N} \times \vec{v}^\perp) & \mathcal{O}_{12} &= \vec{S}_\chi \cdot (\vec{S}_N \times \vec{v}^\perp) \\
\mathcal{O}_6 &= (\vec{S}_\chi \cdot \frac{\vec{q}}{m_N})(\vec{S}_N \cdot \frac{\vec{q}}{m_N}) & \mathcal{O}_{13} &= i(\vec{S}_\chi \cdot \vec{v}^\perp)(\vec{S}_N \cdot \frac{\vec{q}}{m_N}) \\
\mathcal{O}_7 &= \vec{S}_N \cdot \vec{v}^\perp & \mathcal{O}_{14} &= i(\vec{S}_\chi \cdot \frac{\vec{q}}{m_N})(\vec{S}_N \cdot \vec{v}^\perp) \\
\mathcal{O}_8 &= \vec{S}_\chi \cdot \vec{v}^\perp & \mathcal{O}_{15} &= -(\vec{S}_\chi \cdot \frac{\vec{q}}{m_N}) \left[(\vec{S}_N \times \vec{v}^\perp) \cdot \frac{\vec{q}}{m_N} \right]
\end{aligned} \tag{1.1}$$

Unlike the more commonly studied types of interaction (SI,SD), which are not suppressed when $\vec{q} \rightarrow 0$ and for which the scattering rate on nucleons is expected to be largest for low energy nuclear recoils, some of the new EFT operators depend explicitly on \vec{q} and so their interaction

cross section is suppressed for low momentum transfers. Consequently, their scattering rate peaks at non-zero nuclear recoil energy. For sufficiently high WIMP masses, this may even occur outside typical analysis windows, which usually have an upper range of around $43\text{ keV}_{\text{nr}}$ (nuclear recoil equivalent energy) since they are designed to search for SI and SD interactions, which predict exponentially-falling recoil spectra (see Figure ??). Due to the theoretical bias of only considering SI and SD interactions, high energy nuclear recoils remain unexplored in many experiments.

Another typical assumption that can be relaxed is that WIMPs should scatter elastically with nuclei. There exist dark matter models in which the incoming and outgoing WIMPs have different mass states [16] separated by a keV-scale splitting. In the case where the outgoing state is more massive than the incoming state, the cross section for low recoil energies can again be suppressed, this time by scattering kinematics. Recently an inelastic adaptation of the EFT operator framework discussed above was developed [17]. In this case the operators presented in Eqs. 1.1 are modified such that $\vec{v}_{\text{inelastic}}^{\perp} = \vec{v}_{\text{elastic}}^{\perp} + \frac{\delta_m}{|\vec{q}|^2} \vec{q}$. We consider this case in section 2.3.2.

SEARCH FOR HIGH ENERGY NUCLEAR RECOILS IN XENON100 DETECTOR

Standard SI,SD analysis concentrate on energy recoils of up to $O(10)\text{keV}_{\text{nr}}$, hence a hard high energy threshold of is used for them. In XENON100 this threshold value is 43keV_{nr} . However SI and SD are not the only types of interactions possible. These new interactions which predicts higher recoil energies are considered in the EFT framework (see 1.2). moreover a WIMP may have several mass states, which will also result in a possible higher energy recoil.

The EFT framework of [13] is constructed at the WIMP-nucleon level and so each operator may be present independently for protons and neutrons, though UV models can of course correlate their couplings. The full EFT thus has 28 coupling parameters in addition to the WIMP mass, plus a mass splitting δ in the inelastic case. This parameter space is too large to explore in full, so a similar approach to the SI/SD case is taken, assuming only one active operator at a time, considering it equally coupled to protons and neutrons (the “isoscalar” case).

To facilitate the full exploitation of these results by the community, we provide in supplementary material a set of tools for converting any theoretical recoil spectrum dR/dE into an accurate event rate prediction for this analysis, including all detector response and analysis efficiency effects. This may help to set a mildly conservative but quite accurate limit on arbitrary models in the full EFT parameter space, or any other particle dark matter model for which one can supply the expected recoil spectrum. These tools are described further in Appendix A.

In this work we re-analyze science run II data recorded between February 2011 and March 2012, corresponding to 224.6 live days. The characterization of the detector response to ER interactions is performed using dedicated calibration campaigns with ^{60}Co and ^{232}Th radioactive sources, while the response to NR interactions is performed using $^{241}\text{AmBe}$ neutron source calibration campaigns.

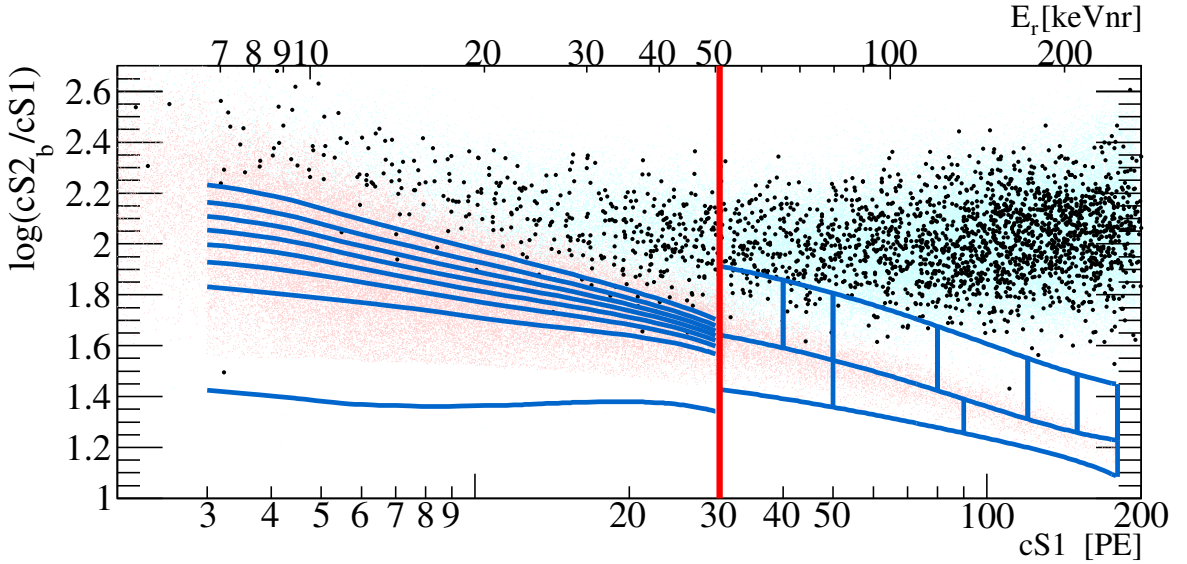


Figure 2.1: Summary of regions of interest, backgrounds, and observed data. ER calibration data, namely ^{60}Co and ^{232}Th data is shown as light cyan dots. NR calibration data ($^{241}\text{AmBe}$) is shown as light red dots. Dark matter search data is shown as black dots. The red line is the threshold between the low and high energy channels. The lines in blue are the bands. For the low-energy channel the bands are constructed to achieve constant expected signal density, and are operator and mass dependent, shown here for a $50 \text{ GeV}/c^2$ WIMP using the \mathcal{O}_1 operator. For the high-energy region, the nine analysis bins are presented also in blue lines.

This work extends the previous results [18, 19], referred to in the following as the low-energy channel, with a new study exploring the recoil energy range between $(43 - 240) \text{ keV}_{\text{nr}}$. The data analysis is divided into two mutually exclusive channels, one optimized for low energies and ranging from $(3-30) \text{ PE}$ in cS1 (low-energy), the other optimized for high energies recoils ranging from $(30-180) \text{ PE}$ in cS1 (high-energy). These two analyses are then combined statistically.

2.1 Low energy channel

This analysis channel relies on the re-analysis of run II data described in [19]. The region of interest (ROI), the background expectation models, data selections and their acceptances are mostly unchanged and so are only briefly summarized here. Differences with respect to said results are highlighted when present.

The ROI for this channel is defined in the $(y, \text{cS1})$ -plane and is shown in Figure 2.1. The lower bound on y corresponds to a 3σ acceptance quantile (as a function of cS1) of a 20 GeV WIMP mass signal model assuming an \mathcal{O}_1 (SI) interaction, while the upper bound is fixed at $y = 2.7$. The range in cS1 is selected as $(3 - 30) \text{ PE}$. The ROI is further divided into eight sub-regions (also called bands) depending on the operator \mathcal{O}_i and on the WIMP mass hypothesis. These bands are arranged to achieve constant expected signal density in each region, as described in [19].

Other than falling into the ROI, an event should fulfill several additional selection criteria (cuts). Data quality and selection cuts are defined to remove events with poor data quality or noisy signals. Events are discarded if they present a time-coincident signal in the outer LXe veto, S2 signals below threshold, multiple-scatters, or are localized outside a predefined fiducial volume of 34 kg. In addition, this analysis channel uses the post-unblinding cuts and data reprocessing described in [19]. More details on these selection criteria and their relative WIMP signals acceptances can be found in [19, 20].

Note that this analysis channel does not employ a variable lower S1 threshold as a function of the event position in the TPC, but instead applies a fixed lower threshold cut on cS1 at 3 PE, conversely to the choice made in [19].

The expected background is modeled separately for ER and NR contributions which are then scaled to exposure and added together. The NR background is estimated by Monte Carlo simulation and accounts for the radiogenic and cosmogenic neutron contributions [21]. The ER background is parametrized as the linear combination of Gaussian-shaped and non-Gaussian components. The former is obtained via a parametric fit of the ^{60}Co and ^{232}Th calibration data, as discussed in [18].

The latter, which consist of anomalous events such as those presenting incomplete charge collection or accidental coincidence of uncorrelated S1s and S2s, is evaluated via dedicated techniques described in [19].

Systematic uncertainties on the background model arising from the Gaussian parametrized fit, and from the normalisations of the NR and non-Gaussian components, have been evaluated and propagated to each band. These errors are small with respect to the statistical uncertainties of each band, which are conservatively taken as the overall uncertainty [19], as discussed in Sec. 2.4.

2.2 High energy channel

This analysis channel targets high energy nuclear recoils and is the focus of this work. The data selection criteria used are based on the criteria described in detail in [20], which were optimized for high acceptance to low energy nuclear recoils. Most of these cuts were found to be fully compatible with (or easily extended) to high energy depositions, however some required more comprehensive studies, which are described in the following .

The width of an S2 pulse increases with the depth (z) of the interaction. This is due to the diffusion of the electron cloud during its propagation through the liquid xenon. Since low energy S2 events show larger spread due to low statistics of drifted electrons, the cut was previously defined in an energy-dependent way. However, for the large recoil energies considered in this channel, this energy dependency is no longer valid. We therefore use here a cut on the S2 width which is a function of the depth of the interaction alone.

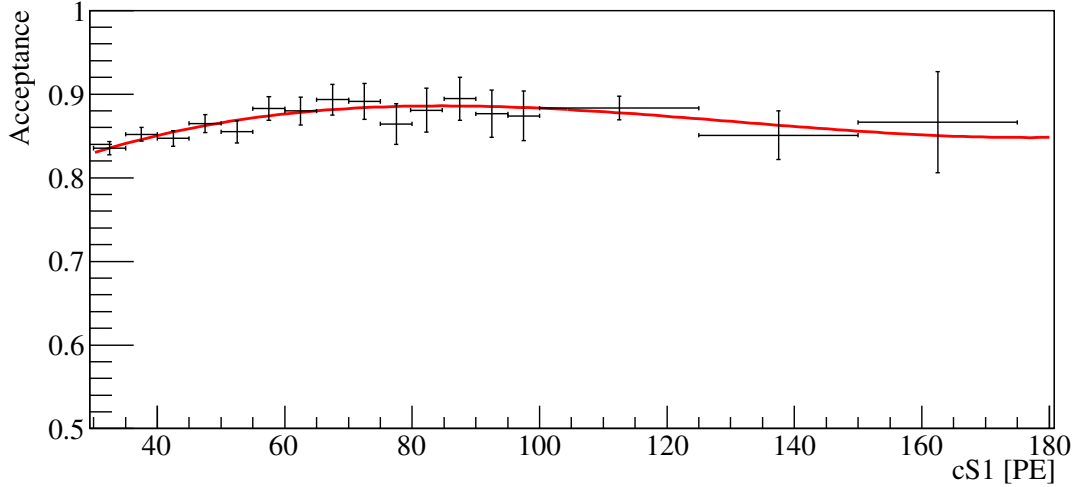


Figure 2.2: The total acceptance of all cuts used. Data from calibration is shown in black, with a 3rd order polynomial fit in red.

As a WIMP will interact only once in the detector, we remove events which have more than one S2. We adopt in this analysis a cut that is more suitable to higher energies and demand a single S2 in a $160\ \mu\text{s}$ window, instead of a linear dependence between the second S2 size and the first.

To define the interaction's exact location in (x, y) , we use several algorithms, one of which is based on a Neural Network (NN) [20]. The NN was not trained to recognize high energy ER events and therefore a cut on the NN reconstruction quality is not suitable for this analysis. We therefore discard this cut but keep all other selections on position reconstruction quality, which is sufficient to ensure a correct position reconstruction.

The total acceptance to WIMP signals is computed based on $^{241}\text{AmBe}$ calibration data as a function of cS1, following the procedure described in [20]. We present this function in Figure 2.2, where the total acceptance is fitted using a third order polynomial.

We define our signal region in the discrimination $(y, \text{cS1})$ -plane using $^{241}\text{AmBe}$ calibration data. The region of interest is shown in Figure 2.1 as blue contour lines. The upper bound in y is defined such that the contribution due to xenon inelastic interaction lines is negligible. The lower bound is defined as the 3σ acceptance quantile of the $^{241}\text{AmBe}$ distribution.

We divide our signal region into two bands in y , constructed such that the $^{241}\text{AmBe}$ data sample is equally distributed in between them. The number of events in each band is ~ 3000 . The bands are further divided into nine bins, the number and boundaries of which have been optimized via Monte-Carlo (MC) simulation. The definitions of the bins boundaries are presented in Table 2.1 and in Figure 2.1.

The main source of background results from ER leakage. We therefore estimate the background distribution in the ROI using ^{60}Co and ^{232}Th calibration events. Contributions from

#	Band	Energy Range (cS1)	# Background Events	# Data Events
1	upper	30 - 40	24±5	20
2	upper	40 - 50	16±3	17
3	upper	50 - 80	12±3	11
4	upper	80 - 120	1.1±0.3	1
5	upper	120 - 150	(1.0±0.5)×10 ⁻¹	1
6	upper	150 - 180	(0.8±0.4)×10 ⁻¹	0
7	lower	30 - 50	0.9±0.3	0
8	lower	50 - 90	(3.5±1.2)×10 ⁻¹	0
9	lower	90 - 180	(1.8±0.7)×10 ⁻¹	0

Table 2.1: Definitions and contents of the analysis bins for the high energy channel. The expected background counts are calculated by taking the calibration sample and scaling it by 6.54×10^{-3} , which is the ratio of observed counts to calibration counts in a sideband.

radiogenic and cosmogenic neutrons, as well as accidental coincidence, are negligible for such a high energy recoil. In Table 2.1 we report the background expectation in the ROI along with the observed events for each bin. Here the background expectation is computed by scaling the calibration sample yield by 6.54×10^{-3} , which is the ratio of observed counts to calibration counts in an independent sideband. The sideband is defined above the upper limit of this analysis and below the ER calibration band mean. Note that in the computation of exclusion limits, the background normalization is fitted to data, rather than using the sideband normalization, as described in section 2.4.

2.3 Signal model

The signal model is produced by taking a theoretical event rate spectrum, the production of which is described in sections 2.3.1 and 2.3.2, and applying the analysis acceptance and detector response as described in [20] to obtain the expected event rate in the detector in terms of detector variables (i.e. cS1, cS2_b). In both analysis channels, we use Eq. 2.1 in order to compute the expected average cS1 for a given NR energy,

$$(2.1) \quad \langle cS1 \rangle = E_{nr} \cdot (L_y \mathcal{L}_{eff}) \cdot \left(\frac{S_{nr}}{S_{ee}} \right)$$

where E_{nr} is the recoil energy, L_y is the average light yield in the detector, \mathcal{L}_{eff} is the scintillation efficiency relative to 122keV_{ee} as a function of E_{nr} , and S_{ee} and S_{nr} are the quenching factors due to the externally applied electric field. Aside from E_{nr} and \mathcal{L}_{eff} these parameters have fixed values, namely $L_y = 2.28 \pm 0.04$, $S_{nr} = 0.95$, and $S_{ee} = 0.58$. Recoils below 3 keV_{nr} are assumed to produce no light. For details of the physics behind these parameters and the construction of the signal probability density function (PDF) please see [19, 20].

For the low-energy region, the expected cS2_b signal is computed following [22] using Eq. 2.2,

$$(2.2) \quad \langle cS2_b \rangle = E_{nr} \mathcal{Q}_y Y$$

where $Y = 8.3 \pm 0.3$ is the amplification factor determined from the detector response to single electrons [23], and \mathcal{Q}_y is the charge yield as a function of E_{nr} . Applying the detector and PMT responses, and the acceptance as in [19], defines the low-energy signal model over the region 3 PE < cS1 < 30 PE, with cS2_b > 73.5 PE as the S2 threshold.

Eq. 2.2 hides a subtlety. The actual cS2_b PDF is composed of two pieces, a Poisson term associated with the initial charge liberation and a Gaussian term associated with the PMT response and other detector effects:

$$(2.3) \quad p_{S2}(cS2_b | E) = \sum_{N'} P_{pmt}(cS2_b | YN', \sigma_Y \sqrt{N'}) \cdot \text{Pois}(N' | \mu_Q)$$

where $\mu_Q = E_{nr} \mathcal{Q}_y$ is the expected number of liberated charges in a nuclear recoil event of energy E , and N' is the actual number of liberated charges. The amplification factor Y is applied to the actual number of liberated charges N' , not the expected number μ_Q . Associated with this is the variance of the Gaussian response PDF, $\sigma_Y \sqrt{N'}$, where in this analysis $\sigma_Y = 6.93$ as measured and described in [23].

For the high energy region we cannot produce the S2 distribution in the same way as the method in [22], since it has not been calibrated for such high recoil energies. We therefore use the NR calibration data distribution in log(cS2_b/cS1) to estimate the WIMP distribution. Above 180 PE in cS1, the event yield of ²⁴¹AmBe data is too low to estimate the distribution accurately. This forms the upper bound of this analysis. With the cS2_b distribution determined by this empirical method, we require only a prediction of the cS1 distribution. This is obtained from Equation (2.1), followed by the application of detector and PMT responses, as well as the acceptance given in Figure 2.2, which completes the high-energy signal model definition.

Figures 2.3 and 2.4 show signal distribution examples for two EFT operators and for the low and the high energy region, respectively. In both cases, the signal distributions are normalized to yield 5 events in the total energy range (low-energy and high-energy).

2.3.1 Elastic scattering

The expected recoil energy spectrum of each WIMP mass for each EFT operator is calculated using the Mathematica package DMFormFactor supplied by Anand et. al. [14, 15]. We use standard assumptions as in previous analyses (e.g [19]) regarding the local dark matter density and velocity distribution, namely $\rho_{\text{local}} = 0.3 \text{ GeV}\cdot\text{cm}^{-3}$ and a Maxwell-Boltzman distribution with a mean given by the local circular velocity $v_0 = 220 \text{ km/s}$ and cut off at an escape velocity of $v_{\text{esc}} = 544 \text{ km/s}$. The responses of xenon nuclei to a scattering event are computed from one-body density matrices provided with the package, in contrast to the Helm form factors which have been used

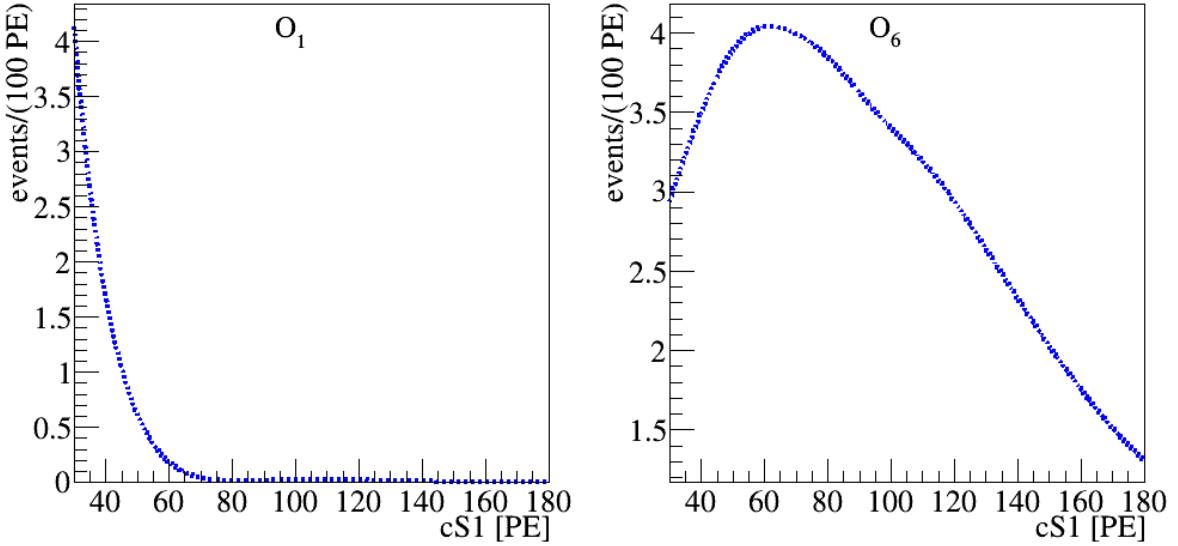


Figure 2.3: The expected signal in the high energy region for a $300 \text{ GeV}/c^2$ WIMP mass, normalized to 5 events. Left(right) is the spectra for $\mathcal{O}_1(\mathcal{O}_6)$. Notice that for \mathcal{O}_1 most of the events are not expected to deposit energy higher than 30 PE whereas for \mathcal{O}_6 a large fraction of the events appear in this region.

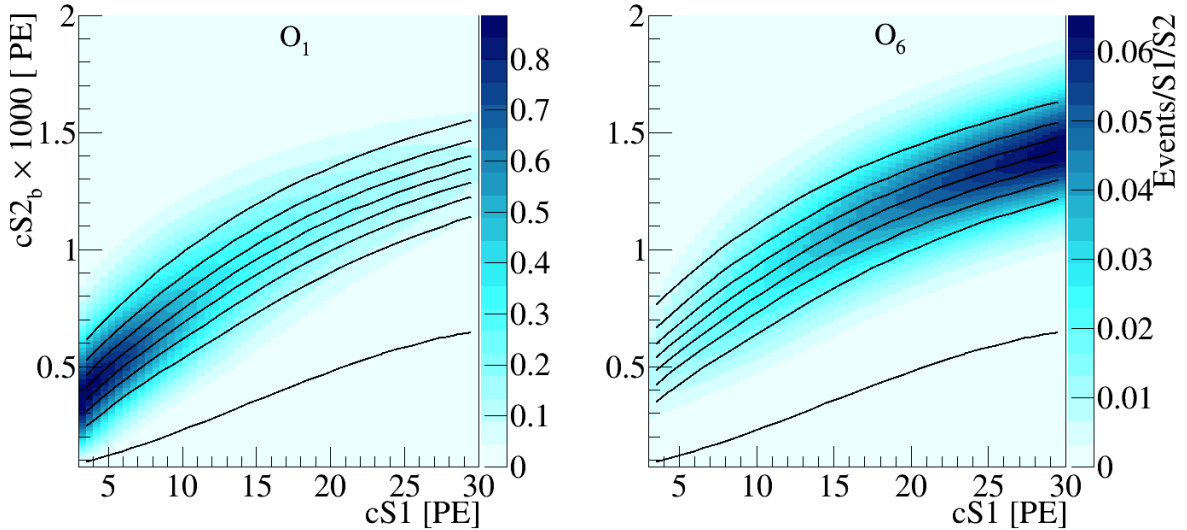


Figure 2.4: The expected signal in the low energy region for a $300 \text{ GeV}/c^2$ WIMP mass, normalized to 5 events. Left(right) is the spectra for $\mathcal{O}_1(\mathcal{O}_6)$. Notice that for \mathcal{O}_1 most of the events are expected to deposit energy lower than 30 PE whereas for \mathcal{O}_6 a large fraction of the events do not appear in this region at all. The black lines indicate the bands constructed on these specific mass and operator models, and are dividing the signal into 8 equally distributed signal sub-regions. This parameter space can be mapped with a one to one mapping to the $(y - cS1)$ space.

in previous analyses. These spectra are produced for the seven most abundant xenon isotopes (128, 129, 130, 131, 132, 134 and 136), combined in proportion to the abundance of these isotopes in the XENON detector [24], then translated into expected signal rates via the method described above.

2.3.2 Inelastic WIMP scattering

To obtain recoil spectra for WIMP-nucleon scattering for all EFT operators with inelastic kinematics, we use a modified version of DMFormFactor provided by Barell et. al. [17]. The authors have modified the original package to enforce the new energy conservation condition $\delta_m + \vec{v} \cdot \vec{q} + |\vec{q}|^2/2\mu_N = 0$, primarily by replacing $\vec{v}_{\text{elastic}}^\perp \rightarrow \vec{v}_{\text{inelastic}}^\perp = \vec{v}_{\text{elastic}}^\perp + \frac{\delta_m}{|\vec{q}|^2} \vec{q}$ in the definitions of the EFT and nuclear operators, giving rise to the well-known minimum velocity for scattering

$$(2.4) \quad v_{\min}/c = \frac{1}{\sqrt{2m_N E_R}} \left| \frac{m_N E_R}{\mu_N} + \delta_m \right|$$

where μ_N is the WIMP-nucleon reduced mass.

Assumptions regarding the dark matter halo and nuclear physics are unchanged. The mass splitting δ_m between dark matter states is varied from (0 – 300) keV, safely beyond the value at which the predicted rate is zero for the entire mass range we consider.

2.4 Statistical inference

The statistical interpretation of data is performed using a binned profile likelihood method, in which hypothesis testing relies upon a likelihood ratio test statistic, \tilde{q} , and its asymptotic distributions [25] to constrain the coupling constants c_k for each operator \mathcal{O}_k . The two analysis channels are combined by multiplying their likelihoods together to produce a joint likelihood function.

$$(2.5) \quad \mathcal{L} = \mathcal{L}_{\text{lowE}(c_i^2, \mathcal{Q}_y, \mathcal{L}_{\text{eff}})} \times \mathcal{L}_{\text{highE}(c_i^2, \mathcal{L}_{\text{eff}})}.$$

Both analyses parametrize the NR relative scintillation efficiency, \mathcal{L}_{eff} , based on existing measurements [26]. Its uncertainty is the major contributor to energy scale uncertainties and is considered as correlated between the two analysis channels via a joint nuisance likelihood term. Throughout this study, all the parameters related to systematic uncertainties are assumed to be normally distributed.

For the low energy channel an extended likelihood function is employed which is very similar to the one reported in [27] and described in detail in [19]. The $(y, cS1)$ -plane is divided into eight WIMP mass dependent bands where events are counted. This binned approach is extended with

the corresponding cS1-projected PDF of each band. The total normalization of the background is fit to data, and an uncertainty is assigned to the relative normalization of each band according to the corresponding statistical uncertainty of the calibration sample.

Signal shape variations due to energy scale uncertainty are modeled via simulation. These include the said \mathcal{L}_{eff} uncertainties and additionally the charge yield uncertainties, which are parametrized based on \mathcal{Q}_y measurement as described in [22].

The low energy likelihood function is shown in Eq. ??,

$$(2.6) \quad \mathcal{L}_{\text{lowE}} = \mathcal{L}_1(c_k^2, \mathcal{L}_{\text{eff}}, \mathcal{Q}_y) \mathcal{L}_2(\epsilon_b) \mathcal{L}_3(\mathcal{L}_{\text{eff}}, \mathcal{Q}_y).$$

$$(2.7) \quad \begin{aligned} \mathcal{L}_1(c_k^2, \mathcal{L}_{\text{eff}}, \mathcal{Q}_y) &= \prod_j \text{Poiss}(n^j | \epsilon_s^j M_s(c_k^2) + \epsilon_b^j M_b) \times \\ &\prod_{i=1}^{n^{i,j}} \frac{\epsilon_s^j M_s(c_k^2) f_s^j(cS1^i) + \epsilon_b^j M_b f_b^j(cS1^i)}{\epsilon_s^j M_s + \epsilon_b^j M_b}, \end{aligned}$$

where f_s^j and f_b^j are the probability density functions of the signal and background respectively in band j . and M_s and M_b are the maximum likelihood estimators for the total number of signal and background events respectively.

$$(2.8) \quad \mathcal{L}_2 = \prod_j \text{Poiss}(n_b^j | \epsilon_b^j N_b)$$

The high energy channel analysis employs a binned likelihood function. Observed and expected event yield are compared in the nine ROI (y , cS1)-bins described in section 2.2. Given the large statistical uncertainty of the background model the above extended likelihood approach is not repeated here. Instead, the maximum likelihood estimation of the background expectation in each bin is constrained by the statistical uncertainty of the calibration sample, while the total normalization is fit to the data. Additionally, to account for potential mis-modeling of the expected background distribution, mainly due to anomalous multiple scatter events, a systematic uncertainty of 20% is assigned independently to each bin. In the high energy channel, uncertainty on the signal acceptance of analysis selections are computed for each signal hypothesis using the parametrized acceptance curve shown in Figure 2.2. Uncertainties on the signal model (y , cS1) distribution due to $^{241}\text{AmBe}$ sample statistical fluctuations, as well as energy scale shape variation due to \mathcal{L}_{eff} uncertainties, are taken into account.

The high energy likelihood function is defined in Eq. 2.9

$$(2.9) \quad \mathcal{L}_{\text{highE}}(c_k^2, \mathcal{L}_{\text{eff}}) = \prod_i \left(\text{Poiss}(n_i^{obs} | n_i^s + n_i^b) \times \text{Gauss}(\eta_i^b) \right) \times \mathcal{L}_{\text{stat}}(\epsilon_j^s, \epsilon_i^b) \times \mathcal{L}_{\text{unc}}^s(\mathcal{L}_{\text{eff}}, A)$$

where the product goes over all 9 bins, ϵ_i^b is the fraction of background event in **bin** i and ϵ_j^s is the fraction of AmBe data in **band** j . This means the uncertainty on the signal is assessed per band. $n_i^s = N_{\text{tot}}^s(c_k^2, \mathcal{L}_{\text{eff}}) \times \zeta_{i,j}^s(\mathcal{L}_{\text{eff}}, \epsilon_j^s)$ is the number of signal events in bin i , $\zeta_{i,j}^s(\mathcal{L}_{\text{eff}}, \epsilon_j^s)$ is the fraction of signal events in bin i which is in band j . $n_i^b = N_{\text{tot}}^{\text{cal}} \times \tau \times \epsilon_i^b(\eta_i^b)$ is the number of background events in bin i . τ is the overall normalization of background to data, and is a free parameter.

2.5 Results

A benchmark region of interest is defined between the upper and lower thresholds in cS1 for each channel. This region is bounded in y -space from above by the $^{241}\text{AmBe}$ NR mean line and below by the lower 3σ quantile of the $^{241}\text{AmBe}$ neutron calibration data. The expected background in the region is $3.0 \pm 0.5_{\text{stat}}$ (low-energy) and $1.4 \pm 0.3_{\text{stat}}$ (high-energy). The number of DM candidates in this benchmark region is 3 (low-energy), and 0 (high-energy). Consequently, the data is compatible with the background-only hypothesis and no excess is found.

For the elastic scattering case, a 90% CL_S [28] confidence level limit is set on the effective coupling constant, c_i , for all operators and masses in the range of $10 \text{ GeV}/c^2$ to $1 \text{ TeV}/c^2$. The c_i are dimensionful, with units of $[\text{mass}]^{-2}$, so we first convert them to dimensionless quantities by multiplying them by $m_{\text{weak}}^2 = (246.2 \text{ GeV})^2$, following the conventions of [14].

These limits are shown in Fig. 2.5 in black, along with limits from CDMS-II Si, CDMS-II Ge and SuperCDMS [1].

For the inelastic scattering case, 90% CL_S confidence level limits on the coupling constants (again scaled by m_{weak}^2) are set. Fig. 2.6 shows limits on the \mathcal{O}_1 (SI) coupling constant as a function of mass splitting and WIMP mass, Fig. 2.7 shows limits for all other operators as a function of the mass splitting δ_m with a fixed WIMP mass of $1 \text{ TeV}/c^2$, projections of results from CDMS-II [29], ZEPLIN-III [30], and XENON100 [31] in the coupling constant and δ_m parameter space are also reported.

For the elastic operator O_1 our results can be compared to those of standard SI analyses by computing the relevant zero-momentum WIMP-nucleon cross-sections. This is not simple to do rigorously because the treatment of nuclear structure used in our analysis is different than in standard analyses, however this difference is small for scattering via O_1 . We can therefore quite safely use the ‘traditional’ correspondence [32]

$$(2.10) \quad \sigma_N^{\text{SI}} = \left(C_1^N \right)^2 \frac{\mu_{\chi,N}^2}{\pi}$$

where $\mu_{\chi,N}$ is the WIMP-nucleon reduced mass. Standard SI analyses assume isospin-conserving interactions, as we do in this analysis, so we can simply set $C_1^N = C_1^0$, such that $\sigma_p^{\text{SI}} = \sigma_n^{\text{SI}}$.

In principle a similar comparison can be done between our limit on the O_4 coupling and standard SD analysis limits, however this time the standard analyses do *not* assume isospin-conserving interactions. Instead they typically assume maximal isospin violation, that is, assuming that WIMPs couple either protons or neutrons. Limits are then derived independently on σ_p^{SD} and σ_n^{SD} . Because of this difference in assumptions, our limits on SD couplings are not directly comparable to usual analyses. However, they can be recast under the appropriate alternate model assumptions using the detector response tables we provide in the supplementary material.

2.5. RESULTS

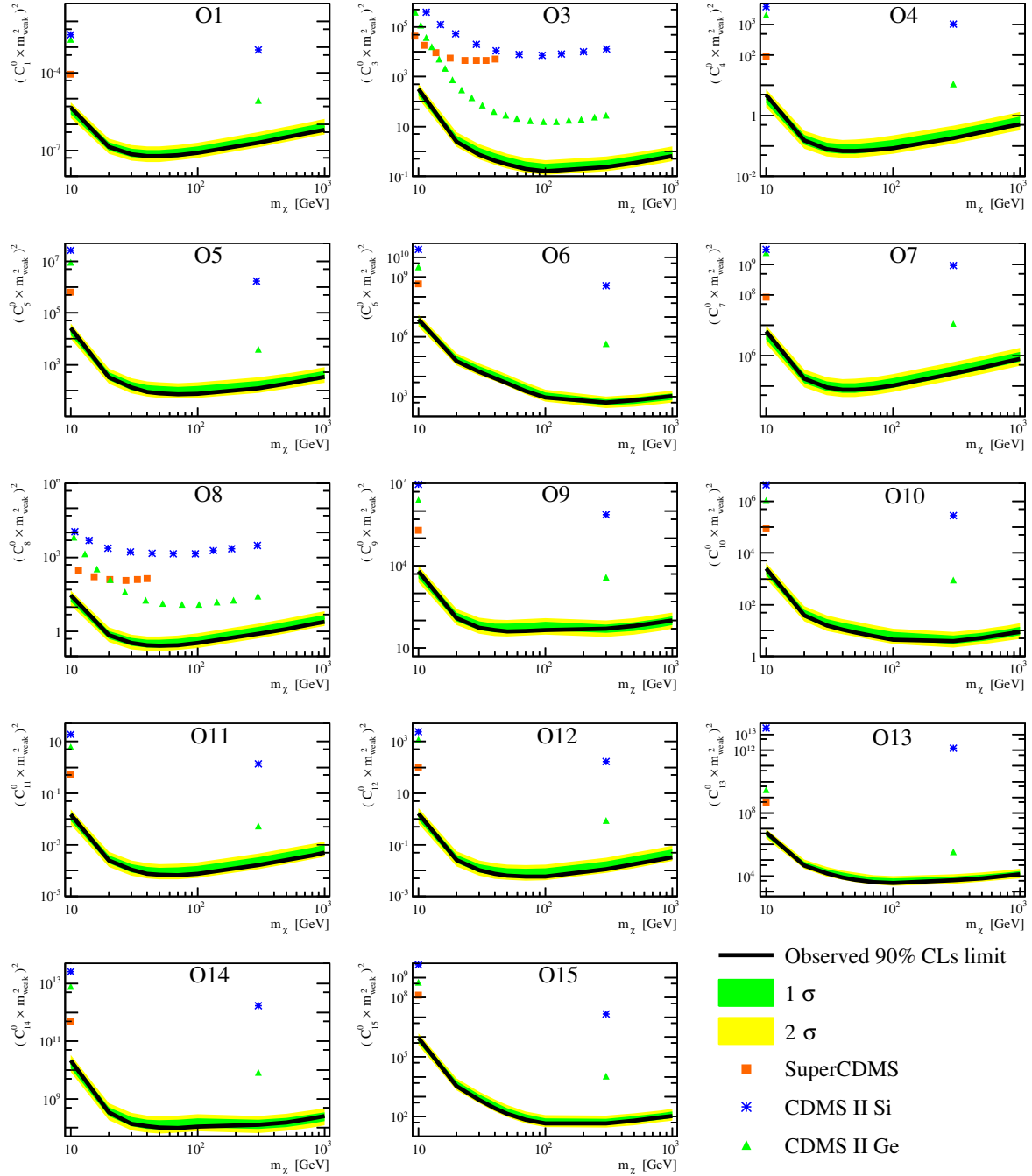


Figure 2.5: The XENON100 limits (90% CL_S) on isoscalar dimensionless coupling for all elastic scattering EFT operators. The limits are indicated in solid black. The expected sensitivity is shown in green and yellow(1 σ and 2 σ respectively). Limits from CDMS-II Si, CDMS-II Ge, and SuperCDMS [1] are presented as blue asterisks, green triangles, and orange rectangles, respectively. For operator 3 and 8 a full limit was published, for all other operators only $m_\chi = 10$ and $m_\chi = 300$ are available.

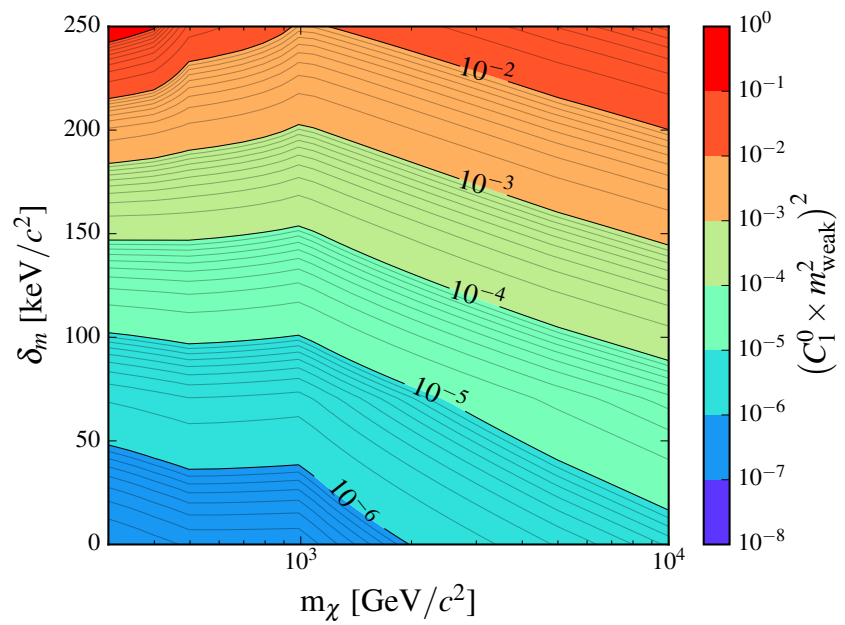


Figure 2.6: 90% CL_S limits, for the inelastic model, on the magnitude of the coupling constant for \mathcal{O}_1 , reported as a function of the WIMP mass and mass splitting δ .

2.5. RESULTS

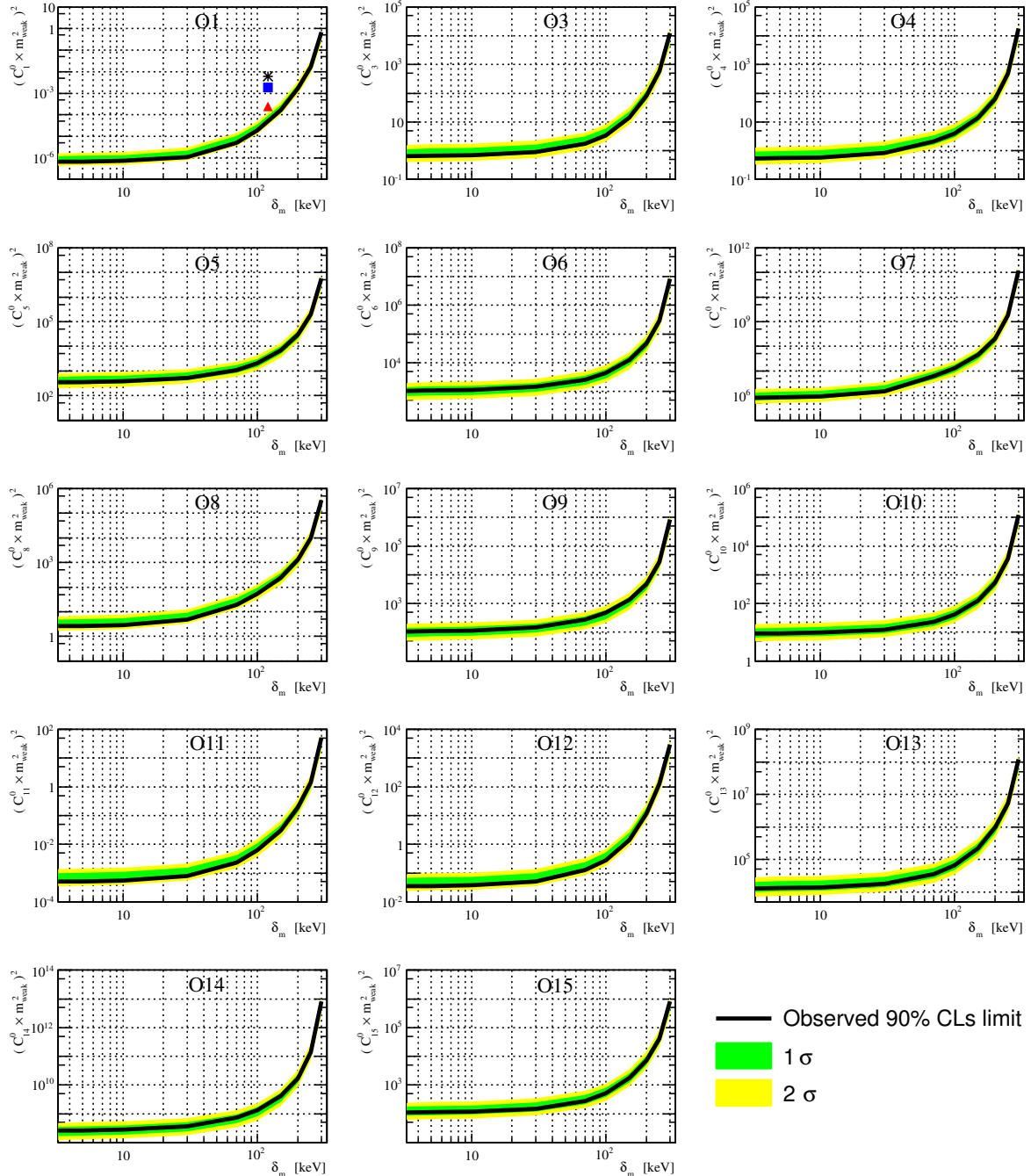


Figure 2.7: The XENON100 90% CL_S limits on a 1 TeV/c² WIMP isoscalar dimensionless coupling constant as function of the WIMP mass splitting δ_m for all inelastic scattering EFT operators. Limits are indicated in solid black. The expected sensitivity is shown in green and yellow (1 σ and 2 σ respectively). For \mathcal{O}_1 (SI) results from XENON100(red triangle) CDMS-II(blue rectangle) and ZEPLIN-III(black star) are overlaid.



EFT SIGNAL MODEL DETECTOR RESPONSE TABLE

In this appendix digital tables which can be used to construct an accurate signal model for the EFT analysis given any input recoil spectrum dR/dE arising from a theoretical model is described. A visualization of the tables is shown in Fig. A.1.

The signal model for the high-energy analysis region can be expressed analytically in the form:

$$(A.1) \quad \frac{dR}{dcS1} = \int \frac{dR}{dE} \cdot \epsilon_{S1}(cS1) \cdot \epsilon_{S2'}(E) \cdot p_{S1}(cS1|E) dE$$

$$(A.2) \quad = \int \frac{dR}{dE} G(cS1, E) dE$$

where $\epsilon_{S1}(cS1)$ and $\epsilon_{S2'}(E)$ represent analysis cut efficiencies, $p_{S1}(cS1|E)$ encodes detector effects, and dR/dE gives the theoretically predicted nuclear recoil rate from WIMP scattering. In the second line we emphasize that all the detector and analysis effects can be encoded in a single function $G(cS1, E)$. To make a signal prediction for the bins in our analysis, this expression needs to be integrated over the appropriate range of $cS1$ for each bin (and divided by two to account for the banding structure in $cS2_b$):

$$(A.3) \quad R_{bin_i} = \frac{1}{2} \int_{lower_i}^{upper_i} \frac{dR}{dcS1} dcS1$$

With some simple rearrangement this rate can be written in terms of an integral over the detector response function G as follows

$$(A.4) \quad R_{bin_i} = \frac{1}{2} \int \frac{dR}{dE} \int_{lower_i}^{upper_i} G(cS1, E) dcS1 dE$$

$$(A.5) \quad = \int \frac{dR}{dE} G'_i(E) dE$$

APPENDIX A. EFT SIGNAL MODEL DETECTOR RESPONSE TABLE

#	E(keV)	bin 1	bin 2	bin 3	bin 4	bin 5	bin 6	bin 7	bin 8	bin 9
3.00e+00	1.44e-22	2.70e-32	1.23e-42	0.00e+00	0.00e+00	0.00e+00	1.44e-22	1.23e-42	0.00e+00	
1.30e+01	9.21e-09	7.58e-14	1.25e-19	6.21e-40	0.00e+00	0.00e+00	9.21e-09	1.25e-19	0.00e+00	
2.30e+01	1.74e-04	1.07e-07	1.24e-11	1.51e-26	0.00e+00	0.00e+00	1.74e-04	1.24e-11	2.64e-32	
3.30e+01	2.22e-02	2.79e-04	6.56e-07	5.47e-18	8.20e-38	0.00e+00	2.25e-02	6.56e-07	1.71e-22	
4.30e+01	1.59e-01	1.68e-02	3.50e-04	1.89e-12	1.24e-28	1.82e-43	1.76e-01	3.50e-04	4.95e-16	
5.30e+01	2.23e-01	1.21e-01	1.40e-02	1.28e-08	6.89e-22	1.43e-34	3.44e-01	1.40e-02	1.82e-11	
6.30e+01	1.10e-01	2.12e-01	9.84e-02	4.73e-06	5.28e-17	5.47e-28	3.21e-01	9.84e-02	2.59e-08	
7.30e+01	2.77e-02	1.54e-01	2.51e-01	2.58e-04	2.20e-13	5.56e-23	1.82e-01	2.51e-01	4.20e-06	
8.30e+01	4.38e-03	6.14e-02	3.67e-01	4.07e-03	1.36e-10	5.26e-19	6.58e-02	3.71e-01	1.65e-04	
9.30e+01	4.65e-04	1.52e-02	3.96e-01	2.73e-02	2.31e-08	1.01e-15	1.57e-02	4.21e-01	2.44e-03	
1.03e+02	3.40e-05	2.47e-03	3.41e-01	9.81e-02	1.50e-06	6.05e-13	2.50e-03	4.21e-01	1.75e-02	
1.13e+02	1.91e-06	2.89e-04	2.29e-01	2.13e-01	4.09e-05	1.22e-10	2.91e-04	3.74e-01	6.77e-02	
1.23e+02	7.75e-08	2.38e-05	1.14e-01	3.28e-01	5.91e-04	1.16e-08	2.39e-05	2.76e-01	1.66e-01	
1.33e+02	2.18e-09	1.33e-06	3.98e-02	3.97e-01	5.03e-03	5.94e-07	1.33e-06	1.55e-01	2.87e-01	
1.43e+02	5.40e-11	6.21e-08	4.06e-02	4.06e-01	2.41e-02	1.42e-05	6.21e-08	6.64e-02	3.74e-01	
1.53e+02	1.33e-12	2.71e-09	2.23e-03	3.66e-01	7.14e-02	1.73e-04	2.71e-09	2.26e-02	4.17e-01	
1.63e+02	2.86e-14	1.00e-10	3.75e-04	2.85e-01	1.51e-01	1.32e-03	1.00e-10	6.04e-03	4.32e-01	
1.73e+02	5.43e-16	3.19e-12	5.09e-05	1.86e-01	2.43e-01	6.76e-03	3.19e-12	1.28e-03	4.34e-01	
1.83e+02	9.29e-18	8.90e-14	5.69e-06	1.01e-01	3.09e-01	2.42e-02	8.90e-14	2.21e-04	4.34e-01	
1.93e+02	1.44e-19	2.21e-15	5.32e-07	4.46e-02	3.23e-01	6.38e-02	2.21e-15	3.14e-05	4.31e-01	
2.03e+02	2.05e-21	4.92e-17	4.23e-08	1.62e-02	2.83e-01	1.29e-01	4.92e-17	3.73e-06	4.28e-01	
2.13e+02	2.71e-23	9.96e-19	2.91e-09	4.89e-03	2.10e-01	2.06e-01	9.96e-19	3.78e-07	4.21e-01	
2.23e+02	3.33e-25	1.85e-20	1.74e-10	1.23e-03	1.31e-01	2.71e-01	1.85e-20	3.29e-08	4.04e-01	
2.33e+02	3.83e-27	3.16e-22	9.25e-12	2.63e-04	6.94e-02	2.99e-01	3.16e-22	2.51e-09	3.69e-01	
2.43e+02	4.16e-29	5.03e-24	4.38e-13	4.80e-05	3.12e-02	2.81e-01	5.03e-24	1.68e-10	3.12e-01	
2.53e+02	4.29e-31	7.48e-26	1.87e-14	7.55e-06	1.20e-02	2.27e-01	7.48e-26	1.00e-11	2.39e-01	
2.63e+02	4.21e-33	1.05e-27	7.23e-16	1.04e-06	3.94e-03	1.58e-01	1.05e-27	5.38e-13	1.62e-01	
2.73e+02	3.95e-35	1.39e-29	2.56e-17	1.25e-07	1.12e-03	9.59e-02	1.39e-29	2.61e-14	9.70e-02	
2.83e+02	3.56e-37	1.74e-31	8.33e-19	1.34e-08	2.77e-04	5.04e-02	1.74e-31	1.15e-15	5.07e-02	
2.93e+02	3.08e-39	2.08e-33	2.51e-20	1.29e-09	6.00e-05	2.31e-02	2.08e-33	4.67e-17	2.31e-02	
3.03e+02	2.58e-41	2.38e-35	7.04e-22	1.11e-10	1.15e-05	9.25e-03	2.38e-35	1.75e-18	9.26e-03	
3.13e+02	2.03e-43	2.61e-37	1.84e-23	8.69e-12	1.95e-06	3.26e-03	2.61e-37	6.06e-20	3.26e-03	
3.23e+02	0.00e+00	2.76e-39	4.54e-25	6.20e-13	2.97e-07	1.01e-03	2.76e-39	1.96e-21	1.01e-03	
3.33e+02	0.00e+00	2.81e-41	1.05e-26	4.06e-14	4.06e-08	2.80e-04	2.81e-41	5.93e-23	2.80e-04	
3.43e+02	0.00e+00	2.72e-43	2.32e-28	2.44e-15	5.04e-09	6.91e-05	2.72e-43	1.69e-24	6.91e-05	

Table A.1: Detector response table using \mathcal{L}_{eff} with constrained scaling parameter set to -1σ value. First column gives recoil energies, subsequent columns give the values of $G'_i(E)$ for each of the 9 high-energy analysis bins. The sampling is in steps of 10 keV_{nr}, which is too coarse to give an accurate signal model for very low WIMP masses, but is suitable for the mass range most relevant to our analysis. Higher resolution $G'_i(E)$ functions, and $G'_i(E)$ functions for other values of \mathcal{L}_{eff} , are given in supplementary material.

where in the last line we absorb the factor of 1/2 into the definition of G'_i . We see here that the signal rate for each bin can be expressed as an integral over the recoil spectrum times a detector response function G'_i for that bin. It is these detector response functions which are shown in Fig. A.1, and which we provide digitally for use by the community. A low-resolution example is given in Table A.1. With these tables it is simple to produce a signal model for our analysis for any theoretical recoil spectrum. The functions G'_i are provided for three values of the nuisance variable \mathcal{L}_{eff} , namely the median value and values at $\pm 1\sigma$ in \mathcal{L}_{eff} . From these, along with the measured background rates given in table 2.1, one may construct a likelihood which accounts for uncertainties in \mathcal{L}_{eff} . Alternatively simply using the -1σ value produces quite an accurate prediction and is generally conservative.

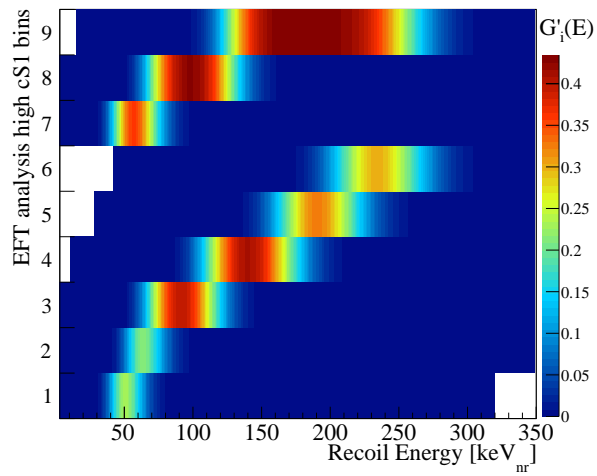


Figure A.1: A visualization of the detector response table for -1σ (i.e. conservative) \mathcal{L}_{eff} , as provided in the supplementary material. The y axis indicates the bins used for the high-energy signal region of this analysis (explained in 2.1). The x axis shows recoil energies, and the colors give the probability density for a recoil of a given recoil energy to produce an event in each analysis bin. To produce a signal model for this analysis, one simply multiplies the table values by dR/dE and integrates over E . The result is the predicted signal rate for each analysis bin.

BIBLIOGRAPHY

- [1] K. Schneck *et al.*, “Dark matter effective field theory scattering in direct detection experiments,” *Phys. Rev.*, vol. D91, no. 9, p. 092004, 2015.
- [2] A. Manzur, A. Curioni, L. Kastens, D. N. McKinsey, K. Ni, and T. Wongjirad, “Scintillation efficiency and ionization yield of liquid xenon for mono-energetic nuclear recoils down to 4 keV,” *Phys. Rev.*, vol. C81, p. 025808, 2010.
- [3] E. Aprile *et al.*, “Measurement of the Scintillation Yield of Low-Energy Electrons in Liquid Xenon,” *Phys. Rev.*, vol. D86, p. 112004, 2012.
- [4] L. Baudis, H. Dujmovic, C. Geis, A. James, A. Kish, A. Manalaysay, T. Marrodan Undagoitia, and M. Schumann, “Response of liquid xenon to Compton electrons down to 1.5 keV,” *Phys. Rev.*, vol. D87, no. 11, p. 115015, 2013.
- [5] D. Muna, “The DRIFT-II directional dark matter detector,” *Nucl. Phys. Proc. Suppl.*, vol. 173, pp. 172–175, 2007.
- [6] C. Deaconu, M. Leyton, R. Corliss, G. Druitt, R. Eggleston, N. Guerrero, S. Henderson, J. Lopez, J. Monroe, and P. Fisher, “Measurement of the directional sensitivity of Dark Matter Time Projection Chamber detectors,” *Phys. Rev.*, vol. D95, no. 12, p. 122002, 2017.
- [7] R. Yakabe, Y. Yamaguchi, K. Miuchi, K. Nakamura, S. Nakaura, T. Hashimoto, T. Ikeda, and R. Taishaku, “Direction-Sensitive Dark Matter Search Using Micro Time-Projection-Chamber,” *JPS Conf. Proc.*, vol. 11, p. 040002, 2016.
- [8] Q. Riffard *et al.*, “MIMAC low energy electron-recoil discrimination measured with fast neutrons,” *JINST*, vol. 11, no. 08, p. P08011, 2016.
- [9] R. H. Dicke, “Coherence in spontaneous radiation processes,” *Phys. Rev.*, vol. 93, pp. 99–110, Jan 1954.
- [10] D. Rosenberger, “Superstrahlung in gepulsten argon-, krypton und xenon-entladungen,” *Physics Letters*, vol. 14, pp. 32–32, Jan. 1965.

BIBLIOGRAPHY

- [11] J. D. Lewin and P. F. Smith, “Review of mathematics, numerical factors, and corrections for dark matter experiments based on elastic nuclear recoil,” *Astropart. Phys.*, vol. 6, pp. 87–112, 1996.
- [12] S. Chang, A. Pierce, and N. Weiner, “Momentum Dependent Dark Matter Scattering,” *JCAP*, vol. 1001, p. 006, 2010.
- [13] A. L. Fitzpatrick, W. Haxton, E. Katz, N. Lubbers, and Y. Xu, “Model Independent Direct Detection Analyses,” 2012.
- [14] N. Anand, A. L. Fitzpatrick, and W. C. Haxton, “Weakly interacting massive particle-nucleus elastic scattering response,” *Phys. Rev.*, vol. C89, no. 6, p. 065501, 2014.
- [15] A. L. Fitzpatrick, W. Haxton, E. Katz, N. Lubbers, and Y. Xu, “The Effective Field Theory of Dark Matter Direct Detection,” *JCAP*, vol. 1302, p. 004, 2013.
- [16] D. Tucker-Smith and N. Weiner, “Inelastic dark matter,” *Phys. Rev.*, vol. D64, p. 043502, 2001.
- [17] G. Barello, S. Chang, and C. A. Newby, “A Model Independent Approach to Inelastic Dark Matter Scattering,” *Phys. Rev.*, vol. D90, no. 9, p. 094027, 2014.
- [18] E. Aprile *et al.*, “Dark Matter Results from 225 Live Days of XENON100 Data,” *Phys. Rev. Lett.*, vol. 109, p. 181301, 2012.
- [19] E. Aprile *et al.*, “XENON100 Dark Matter Results from a Combination of 477 Live Days,” *Phys. Rev.*, vol. D94, no. 12, p. 122001, 2016.
- [20] E. Aprile *et al.*, “Analysis of the XENON100 Dark Matter Search Data,” *Astropart. Phys.*, vol. 54, pp. 11–24, 2014.
- [21] E. Aprile *et al.*, “The neutron background of the XENON100 dark matter search experiment,” *J. Phys.*, vol. G40, p. 115201, 2013.
- [22] E. Aprile *et al.*, “Response of the XENON100 Dark Matter Detector to Nuclear Recoils,” *Phys. Rev.*, vol. D88, p. 012006, 2013.
- [23] E. Aprile *et al.*, “Observation and applications of single-electron charge signals in the XENON100 experiment,” *J. Phys.*, vol. G41, p. 035201, 2014.
- [24] E. Aprile *et al.*, “Limits on spin-dependent wimp-nucleon cross sections from 225 live days of xenon100 data,” *Physical review letters*, vol. 111, no. 2, p. 021301, 2013.
- [25] G. Cowan, K. Cranmer, E. Gross, and O. Vitells, “Asymptotic formulae for likelihood-based tests of new physics,” *Eur. Phys. J.*, vol. C71, p. 1554, 2011. [Erratum: Eur. Phys. J.C73,2501(2013)].

BIBLIOGRAPHY

- [26] E. Aprile *et al.*, “Dark Matter Results from 100 Live Days of XENON100 Data,” *Phys. Rev. Lett.*, vol. 107, p. 131302, 2011.
- [27] E. Aprile *et al.*, “Likelihood Approach to the First Dark Matter Results from XENON100,” *Phys. Rev.*, vol. D84, p. 052003, 2011.
- [28] A. L. Read, “Modified frequentist analysis of search results (The CL(s) method),” in *Workshop on confidence limits, CERN, Geneva, Switzerland, 17-18 Jan 2000: Proceedings*, pp. 81–101, 2000.
- [29] Z. Ahmed *et al.*, “Dark Matter Search Results from the CDMS II Experiment,” *Science*, vol. 327, pp. 1619–1621, 2010.
- [30] D. Yu. Akimov *et al.*, “Limits on inelastic dark matter from ZEPLIN-III,” *Phys. Lett.*, vol. B692, pp. 180–183, 2010.
- [31] E. Aprile *et al.*, “Implications on Inelastic Dark Matter from 100 Live Days of XENON100 Data,” *Phys. Rev.*, vol. D84, p. 061101, 2011.
- [32] A. De Simone and T. Jacques, “Simplified models vs. effective field theory approaches in dark matter searches,” *Eur. Phys. J.*, vol. C76, no. 7, p. 367, 2016.

